MIT Libraries | DSpace@MIT

MIT Open Access Articles

Optimal shape and motion of undulatory swimming organisms

Massachusetts Institute of Technology

Optimal shape and motion of undulatory swimming organisms

Grgur Tokić,[1] Dick K.P. Yue[1*]

[1]*Department of Mechanical Engineering, Massachusetts Institute of Technology,*

Cambridge, MA 02139, USA

[*]To whom correspondence should be addressed; E-mail: yue@mit.edu.

Abstract

Undulatory swimming animals exhibit diverse ranges of body shapes and motion patterns and are often considered as having superior locomotory performance. The extent to which morphological traits of swimming animals have evolved due to primarily locomotion considerations is, however, not clear. To shed some light on that question, we present here the optimal shape and motion of undulatory swimming organisms obtained by optimising locomotive performance measures within the framework of a combined hydrodynamical, structural and novel muscular model. We develop a muscular model for periodic muscle contraction which provides relevant kinematic and energetic quantities required to describe swimming. Using an evolutionary algorithm, we performed a multi-objective optimisation for achieving maximum sustained swimming speed U and minimum cost of transport COT — two conflicting locomotive performance measures that have been conjectured as likely to increase fitness for

1

survival. Starting from an initial population of random characteristics, our results show that, for a range of size scales, fish-like body shapes and motion indeed emerge when U and COT are optimised. Inherent boundary-layer-dependent allometric scaling between body mass and kinematic and energetic quantities of the optimal populations is observed. The trade-off between U and COT affects the geometry, kinematics and energetics of swimming organisms. Our results are corroborated by empirical data from swimming animals over nine orders of magnitude in size, supporting the notion that optimising U and COT could be the driving force of evolution in many species.

Keywords: biomechanics; optimal morphology; undulatory swimming; scaling; multi-objective optimisation

1. Introduction

Undulatory swimming organisms achieve locomotory feats that in terms of maximal burst speed, acceleration, or agility are unmatched by man-made aquatic vehicles. These have been the inspiration for the development of biomimetic robots [1] which were reverse-engineered based on living fish under the assumption that their morphology is optimised for swimming. Whether fish-like organisms are indeed optimised for swimming, and whether extant morphological traits would evolve based on locomotion considerations alone, however, has not been completely established.

Despite a vast body of work on various aspects of undulatory swimming (from physiology to physics of swimming), optimisation studies based on mathematical models are relatively sparse. Swimming motion for a given body shape has been optimised from a hydrodynamical perspective using theoretical [2] and numerical models [3, 4]. The body shape and body stiffness for efficient hydrodynamical performance have also been studied [5]. Further insights into the relationship between morphology and swimming performance have been obtained from numerical studies on bodies of prescribed shape and motion [6–8], but without conducting optimisation.

A significant drawback of all these studies is that they do not consider muscle behaviour and the

associated energetics so that it is not clear whether the motions or morphologies obtained are physiologically feasible. Mathematical models of muscle behaviour during swimming have mostly been developed to study the muscle response to a given neural activation [9–12], with model parameters being often fine-tuned for particular species [12–14]. The actuation–response relationship varies widely among species [15–17], making these models unsuitable for the optimisation of morphological traits of a generic organism. Furthermore, these models do not provide information about metabolic energy consumption which is a critical component of swimming energetics.

A different approach to studying morphological effects on swimming, without resorting to detailed mechanistic models, is through a comparison of extant morphologies based on their observed performance. Qualitative studies of fish shapes [18–21] and hypothesis testing methods [22, 23] have given us some intuition of the optimal body shapes and motion patterns of undulatory swimmers and have provided insight into the effects that performance trade-offs can have on morphology. These methods, however, are qualitative and generally not predictive.

In contrast to the existing studies, our objective is to *predict* optimal morphological traits, including body shapes and motion patterns, across broad ranges of size scales. We achieve this by optimising locomotory performance measures based on a comprehensive swimming model which incorporates a novel model for periodic muscle contraction. We perform multi-objective optimisation with respect to two conflicting performance measures (sustained swimming speed U and cost of transport COT) to understand the effect of the interplay between them on the morphological traits of the obtained optimal organisms. Finally, the obtained optimal morphological traits are compared to those observed in nature.

2. Model description

We study sustained straight-line undulatory swimming (powered by superficial red muscle [20, 24, 25]), where an organism passes a muscle-produced wave of curvature down its body and propels

itself using the hydrodynamic forces exerted on the body as a reaction to the motion. To describe the kinematics and energetics of swimming, the main components of the swimming machine converting the energy from food into useful propulsion work have to be modelled. In addition to an effective and robust body shape and motion description, our swimming model consists of three parts: (i) hydrodynamical model describing the flow around the moving body, (ii) structural model describing the distribution of the internal forces required for swimming motion, and (iii) muscle model describing the muscle behaviour needed to achieve such forces. To facilitate optimisation, these model components are sufficiently general to describe the physics for arbitrary morphologies across many scales, and highly computationally efficient to allow a large number of simulation realisations.

(a) Body and motion description

We consider an arbitrary three-dimensional organism of mass m characterised by its body length L, tail height D and body width B, figure 1. We assume that the body is symmetric with respect to the horizontal and vertical planes, with elliptical cross-sections of area $A(x)$ and sectional moment of inertia $I(x)$. The lengths of axes of cross-sections determine the body height and width distributions, denoted by $d(x)$ and $b(x)$, respectively. Wetted surface of the body is denoted by S. The body is assumed to be neutrally buoyant, with uniform body density ρ, for simplicity. Neutrally buoyant fish often hold the fins close to the body during steady undulatory swimming [15], thus minimising their effect on the flow around the body. In this paper, we therefore do not consider fins and other appendages.

The locomotory muscle is made of red muscle fibres arranged in a superficial longitudinal strip [20, 25], located along the horizontal symmetry plane on each side of the body, figure 1a, b. The muscle cross-section $A_m(x)$ is a small portion μ_0 ($\mu_0(x) = 2A_m(x)/A(x)$) of the body cross-section $A(x)$ [9, 25].

We express the undulatory motion of the body neutral line $\hat{h}(x, t)$ using a single time harmonic

[15, 20, 24]:

$$\hat{h}(x,t) = r(x)\cos(2\pi x/\lambda_b - \omega t) \,, \tag{1}$$

where ω is the angular frequency of tail-beat (with tail-beat period $T = 2\pi/\omega$), $r(x)$ is the deformation envelope and λ_b the wavelength of the body undulation.

(b)   Hydrodynamical model

The role of a hydrodynamical model is to determine the relationship between the swimming speed U and the tail-beat frequency ω for steady swimming, and to provide external forces that occur during swimming. We are interested in swimming at high Reynolds numbers $Re \equiv U\,L/\nu$ (ν is the kinematic viscosity of water), for which potential flow models can be used. We use classic Lighthill's potential flow slender-body model for small-amplitude motion [26], which has the advantage of being three-dimensional and very simple to solve compared to other numerical models.

The hydrodynamic pressure field around a freely swimming body gives rise to a forward pointing thrust force F_T powering the forward motion, and a lateral force $F_L(x,t)$ which causes an additional rigid-like lateral movement known as recoil. Both the imposed motion $\hat{h}(x,t)$ and the recoil are assumed to be small (compared to L), so the total deflection h of the body can be written as $h(x,t) = \hat{h}(x,t) + y_0(t) + x\,\phi(t)$, where $y_0(t)$ is the lateral and $\phi(t)$ the angular recoil, figure $1c$. Equations of motion of a swimming body as a whole, relating the lateral (angular) acceleration and the total external force (moment) acting on the body, provide a way to calculate the unknown lateral (angular) recoil:

$$\begin{aligned}
\int_0^L \rho A \frac{\partial^2 h(x,t)}{\partial t^2}\,dx &= -\int_0^L F_L(x,t)\,dx \\
\int_0^L x\rho A \frac{\partial^2 h(x,t)}{\partial t^2}\,dx &= -\int_0^L x F_L(x,t)\,dx \,,
\end{aligned} \tag{2}$$

where, for a slender body, $F_L(x,t) = \mathcal{D}\left(m_a(x)\,\mathcal{D}\,h(x,t)\right)$ [26]. Here $\mathcal{D} \equiv \partial_t + U\partial_x$ is the material

109   derivative and $m_a(x)$ the cross-sectional added mass.

110   To obtain the steady swimming speed U in the present context, we follow a standard approach [4, 26, 27] wherein one equates the average thrust $\overline{F_T}$ from a potential flow model with the average drag $\overline{F_D}$ calculated from an empirical relationship, i.e. requiring $\overline{F_T} = \overline{F_D}$. For Lighthill's slender-body model [26], $\overline{F_T} = \frac{1}{2}m_a(L)\left[\overline{(\partial_t h)^2} - U^2\overline{(\partial_x h)^2}\right]_{x=L}$. The drag force is modelled as $\overline{F_D} = 0.5\rho U^2 S C_D$, using an empirical formula for the drag coefficient $C_D = C_D(Re)$ (see electronic supplementary material, eq. (S.11), [27]), which exhibits a discrete jump transitioning from laminar to turbulent regime. Although there is some uncertainty about the accuracy of C_D, proper scaling with Re is more important for this study than its exact value.

118   The solution of the nonlinear system of equations ((2), $\overline{F_T} = \overline{F_D}$) determines the steady swimming condition, which can be expressed in terms of ω–U or ω–Re relationship since for a given organism L is known.

(c)   Structural model

122 The main purpose of the structural model is to obtain the internal forces acting in a swimming body so that the muscular activity required for powering the motion could be calculated. This is modelled using the standard Euler-Bernoulli beam equation [28]

$$\rho A(x)\frac{\partial^2 h}{\partial t^2} + \frac{\partial^2}{\partial x^2}\left(EI(x)\frac{\partial^2 h}{\partial x^2}\right) +$$

$$+ \frac{\partial^2}{\partial x^2}\left(\nu_b I(x)\frac{\partial^3 h}{\partial t \partial x^2}\right) + F_L = \frac{\partial^2 M}{\partial x^2}\ . \quad (3)$$

125 The above terms, corresponding respectively to forces due to inertial, elastic, visco-elastic, hydrodynamic effects, are all balanced by the bending moment M produced by muscles. Aggregate Young's modulus E and visco-elastic coefficient ν_b include combined contribution from all the passive elements during bending: elasticity and visco-elasticity of the spine, the skin, the white

muscle and the inactive part of red muscles (assuming that the morphology of the organisms is equivalent to that of fish).

Assuming there are no muscles at the very ends of the body ($M(x = 0, L; t) = 0$), the boundary conditions that a feasible $h(x, t)$ has to satisfy require [28]

$$\frac{\partial^2 h}{\partial x^2} = 0, \qquad \frac{\partial^3 h}{\partial x^3} = 0, \qquad x = 0, L . \tag{4}$$

The sectional bending moment $M(x, t)$ can then be directly obtained from (3) for a given $h(x, t)$ which satisfies (4). A muscle model has to be introduced to answer the question how precisely the required bending model M is achieved.

(d) Muscle model

The primary purpose of a muscle model is to determine the physiological feasibility of the pre-scribed motion and to determine the energy consumption by the muscle, which highly affects swimming energetics (the energy losses in real fish muscles are significant and amount to a muscle efficiency of around 20% [27]). The present model is developed for periodic swimming powered by red muscle, as is generally the case in sustained fish swimming [20, 24, 25]. Other modes of swim-ming, e.g. unsteady burst-and-glide swimming in which white muscle fibres are recruited [29], are not considered here. The model should, however, correctly describe the most important character-istics of muscle behaviour and be valid for different undulatory-swimming species and across the scales. We have focused on the facts that seem to be universally valid for swimming fish and have built a new model based on them.

The contractive force $F_{musc}(x, t)$ that the muscles at some cross-section have to provide can be obtained from the calculated required bending moment $M(x, t)$. For a muscle of small cross-section placed $1/2 b(x)$ from the neutral line, this corresponds to $F_{musc}(x, t) = M(x, t)/0.5 \, b(x)$. Since the muscle produces contractive forces only, in alternating manner from side to side at any

x [20, 30], the sign of F_{musc} uniquely determines the side of the active muscle fibres. According to our definition, the required contractive force F_{musc} is positive/negative when the muscles on the right/left side of the body are active.

The force F_{fib} that each muscle fibre actually produces is a function of the fibre kinematics, which is in turn dependent on body motion. Such dependence is also true for the metabolic power P_{fib} consumed per fibre length. During steady swimming, it can be assumed that muscle behaviour is quasi-steady [15, 31] since the characteristic time for muscle fibres to adapt to a new force is typically much shorter than the characteristic tail-beat period T. Thus, we assume that for a contracting fibre, F_{fib} and P_{fib} are functions of instantaneous contraction velocity $v(x, t)$, given by Hill's model [31] (see electronic supplementary material, section 3.2).

The contraction velocity $v(x, t)$ of superficial muscle fibres (measured in lengths/second) can be determined from the time rate of change of fibre strain, which in turn can be determined from the curvature of the neutral line alone [9, 15, 24, 32]. Based on a simple beam theory [15, 24],

$$v(x, t) = \pm \frac{1}{2} b(x) \frac{\partial}{\partial t} \left(\frac{\partial^2 h}{\partial x^2} \right) \ . \tag{5}$$

The sign of F_{musc} determines the choice of plus-minus sign in (5), where plus(minus) corresponds to the case when the fibres on the right(left) side of the body are active (the active side of the body cannot be determined from the rate of change of curvature of the spine alone).

Non-dimensional relative contraction velocity is defined as $v_r(x, t) \equiv v(x, t)/v_{max}$, where v_{max} is maximal achievable contraction velocity for given fibre characteristics.

At any cross-section, the required muscle force F_{musc} is the sum of all the active single-fibre contractive forces F_{fib}. To obtain the required force $F_{musc}(x, t)$ constrained by $F_{fib}(v(x, t))$, we assume that only a fraction $\mu(x, t)$ of the total muscle cross-section area $A_m(x)$ is activated:

$$\mu(x, t) = \frac{F_{musc}(x, t)}{F_{fib}(v(x, t)) A_m(x)} \ , \quad |\mu(x, t)| \leq 1 \ . \tag{6}$$

172 The condition for a physiologically feasible motion $h(x, t)$ can then be stated as

$$|\mu| \leq 1, \quad |v_r| \leq 1, \quad \forall\, x, t\,. \tag{7}$$

173 The metabolic power consumption per unit length of the muscle $P_{musc}(x, t) = A_m(x)\,|\mu(x, t)|\,P_{fib}(v(x, t))$

174 is proportional to the active muscle portion. It is always positive, corresponding to the fact that

175 metabolic energy is being spent when the mechanical power output of the muscle $P_{mech}(x, t) =$

176 $F_{musc}(x, t)v(x, t)$ is positive or negative, regardlessly. With the muscle force and power consump-

177 tion calculated, all relevant dynamic and energetic quantities for locomotion can be calculated.

178 The predicted muscle efficiency matches the measured one for swimming fish and for isolated red

179 fibres (see electronic supplementary material, section 3.3).

180 # 3.   Performance measures and optimisation variables

181 The optimisation problem we are trying to solve can be stated as follows: find optimal solutions

182 for a set of conflicting objectives (locomotory performance measures) over the variables that ade-

183 quately parametrise the body shape and motion, constrained by the motion feasibility (7) and shape

184 integrity conditions. Body shape and motion parameters are chosen as the optimisation variables

185 since they are the key mechanistic components that determine locomotory performance.

186 To elucidate the trade-offs between conflicting locomotion-based objectives, we focus on two

187 performance measures of arguably great importance in the evolutionary scenario [20, 33]: max-

188 imising sustained swimming speed and minimising energy consumption. For the latter, we use a

189 standard nondimensional measure called cost of transport COT [20, 34] (for derivation, see elec-

190 tronic supplementary material, section 5):

$$COT \equiv \frac{\overline{P_{tot}}}{mgU} = \frac{P_s + \overline{P_{musc}^L}}{mgU} \tag{8}$$

where $\overline{P_{tot}}$, the total metabolic power consumed by swimming at speed U, is the sum of the metabolic power $\overline{P_{musc}^L}$ consumed by swimming muscles and the standard metabolic rate P_s required for other physiological processes even when there is no motion at all ($\overline{(\cdot)^L}$ denotes a length-integrated, time-averaged quantity). Note that in (8), gravity g is used merely for nondimensionalisation and is not related to swimming. Expressed by (8), COT is the "gallons-per-mile" measure quantifying the total energy consumption per unit mass and distance, which probably governs long migrations [20].

The choice of locomotive performance measures to optimise is not unique. For example, an energetic measure can be a generic power coefficient defined as $C_P \equiv \overline{P_T}/P_0$, where $P_0 \equiv 0.5\rho S U^3$, and $\overline{P_T}$ is some measure of swimming power based on which C_P has different meanings and implications. In general, C_P might be more suited for studying the efficacy of hydrodynamical propulsion itself as it is normalised by the scale of hydromechanical power P_0. The ultimate justification of the present choice of U and COT has to be borne out on whether the consequent predictions based on it are corroborated by nature.

Optimising conflicting objectives usually leads to an infinite number of optimal solutions. Since by the definition of conflicting objectives an organism cannot be optimal in every objective, it is considered as optimal when it is non-dominated [35], i.e. when there is no (feasible) variation of organism's morphology that could improve every objective. We call the set of non-dominated organisms the optimal population Π.

To facilitate the optimisation of generic swimming geometries and motions, we parametrise the body height, width, and motion along the body in terms of general unbiased mathematical descriptions. We represent the body height distribution $d(x)/L$ by a sum of $N_S + 1$ polynomial shape functions D_n

$$d(x)/L = D/L\bigg(\sqrt{x/L} + \sum_{n=0}^{N_S} C_n D_n(x/L) \bigg) \,,$$

$$D_n(x) = T_n(2x-1) - T_{n+2}(2x-1) \,,$$

(9)

where $T_n(x)$ is the Chebyshev polynomial of the first kind of order n; shape coefficients C_n produce different shapes when varied. Without loss of generality, we assume the body width $b(x)$ to be given by a symmetrical NACA-00 profile with relative maximum thickness B/L. We thus parametrise the body shape by $N^S = N_S + 3$ optimisation variables (D/L, B/L, $C_0,\ldots,C_{N_S+1}$). The body length L is not a parameter as it can be calculated for a given m once $d(x)/L$ and $b(x)/L$ are prescribed.

The spatial and temporal parametrisation of body motion $\hat{h}(x,t)$ is achieved using $N^M = N+1$ variables. The envelope $r(x)$ is represented as a sum of N Chebyshev polynomials, where the coefficients of the series serve as optimisation variables (see electronic supplementary material, section 1.2). To reduce the number of optimisation variables and to ensure the validity of Lighthill's model (see electronic supplementary material, section 4), we set the relative body-undulation wave length to $\lambda_b/L = 1$, a value characteristic for many fishes [15, 20, 27]. Upon parametrisation, the motion is slightly corrected to satisfy motion boundary conditions (4).

The swimming speed U and the tail-beat period T can both be determined from Re using the steady swimming condition. Hence, we use Re as a kinematic optimisation variable and the values of U and T (or ω) are determined as the outcome of optimisation.

In the following, we use $N^S = N_S + 3 = 5$ and $N^M = N + 1 = 4$ as we have found that those values are sufficient to represent the extant body shapes and motion patterns to within $O(1\%)$. The advantage of our parametrisation is that, despite N^S and N^M being small, we are capable of representing a large variety of shapes and motion patterns without introducing a particular bias.

4. Results

We optimise for U and COT using a multi-objective evolutionary algorithm [36], evolving generations of feasible populations starting from the one with random body shape and motion parameters. We perform calculations for body sizes ranging from $m = 0.001$ kg to $m = 1{,}000{,}000$ kg to obtain

the optimal populations $\Pi(m)$, figure 2. Given the conflicting nature of optimisation objectives, $\Pi(m)$ obtains a range of values for each swimming characteristic presented (Re, U, COT, T, relative tail amplitude h_T/L, μ_{max}). The results are compared with the empirical data, where available, for fish and cetaceans.

For specificity, in this discussion we focus on the values attained by organisms for which either U or COT is optimal. Hereafter, these predicted values are denoted as $(\cdot)_{U-opt}$ and $(\cdot)_{COT-opt}$ for those corresponding to $U-$ and $COT-$optimal organisms, respectively. As discussed earlier, the choice of performance measure for optimisation is not unique. For comparison, we provide results for the minimisation of power coefficients, namely of power-output-based $C_P^M \equiv \overline{P_{mech}^L}/P_0$ (used in [14]) and of power-consumption-based $C_P^T \equiv \overline{P_{musc}^L}/P_0$ (suggested in [39]).

The Reynolds number Re employed by the optimal populations Π grows over four orders of magnitude, figure 2a. The prominent feature of $Re - m$ relationship is the presence of a transition region $\mathcal{R}_T$ separating otherwise allometric relationships (visible from the linear $(Re)_{U-opt} - m$ or $(Re)_{COT-opt} - m$ relationships in log–log plots). The transition regions $(\mathcal{R}_T)_{U-opt}$ and $(\mathcal{R}_T)_{COT-opt}$ are defined as the range of m for which U-optimal and COT-optimal organisms swim at speeds just below critical Reynolds number Re_{cr} to remain in the laminar regime. The ranges of $(\mathcal{R}_T)_{U-opt}$ and $(\mathcal{R}_T)_{COT-opt}$ differ, reflecting the earlier transition to turbulent flow of U-optimal organisms $((Re)_{U-opt} > (Re)_{COT-opt}$ for a given m). Different behaviour in $\mathcal{R}_T$, accompanied with the change of $(\cdot)_{U-opt} - m$ and $(\cdot)_{COT-opt} - m$ slopes over it, is a common feature of almost all quantities describing $\Pi(m)$ (some shown in figure 2).

The optimised swimming speed U obtains values from $O(0.1 - 1)$ m/s (corresponding to relative swimming speed U/L in body-lengths/s from $O(1)$ to $O(0.1)$, figure S12a). As one of the performance measures being optimised, U is clearly maximal(minimal) for U-optimal(COT-optimal) organisms in Π of all body sizes, as expected. We find a decrease in slopes of $(U)_{U-opt} - m$ and $(U)_{COT-opt} - m$ over $\mathcal{R}_T$, as has been previously suggested [21, 37], figure 2b. The slight decrease of $(U)_{U-opt}$ in the transition region $(\mathcal{R}_T)_{U-opt}$ is due to the organism's inability to cross the

laminar-to-turbulent transition with the available muscle. A similar, but more pronounced decrease of $(U)_{COT-opt}$ in the transition region $(\mathcal{R}_T)_{COT-opt}$ can be explained by energetic arguments: here more muscle units could be employed but that would result in undesirably higher COT.

The cost of transport COT (figure 2c) is one of the quantities that heretofore could not be predicted from theoretical or numerical considerations due to the lack of a comprehensive muscle model. The results we obtain show a slight general under-prediction of the COT range which might imply that the values of P_s or ν_b we use might be lower than those in many natural organisms.

The obtained tail-beat period T in the laminar regime seems to be slightly greater than the measured one (but of the same order), figure 2d. Over the entire m-range, $(T)_{COT-opt} > (T)_{U-opt}$ consistently. We find that the increase in T with m is correlated with the decrease in maximum $\max v_r$, as has also been empirically found for cyclical muscle contractions [40] (figure S12c). Note that even for the smallest organisms investigated, $T > 0.1$ sec (figure 2d) which is greater than the 30ms–50ms needed for the muscle fibre to adapt to a new force [15], thus not violating the quasi-steady assumption.

The relative tail amplitude h_T/L shows a decreasing trend in each of the sub-regions, figure 2e. Generally, $h_T/L \ll 1$, which does not violate our small-amplitude motion assumption. A non-obvious prediction is the fact that $(h_T/L)_{U-opt} < (h_T/L)_{COT-opt}$ below $\mathcal{R}_T$ but $(h_T/L)_{U-opt} > (h_T/L)_{COT-opt}$ above $\mathcal{R}_T$.

The maximum active muscle portion μ_{max}, i.e. the maximum value of $\mu(x,t)$, exposes some of the driving constraints behind the obtained overall results, figure 2f. As expected, $(\mu_{max})_{U-opt} = 1$ for all m, limiting the maximal achievable swimming speed. Generally, $(\mu_{max})_{COT-opt} < 1$ indicating that only a portion of the muscles is required, as suggested [41].

Compared to these results, it appears that power-output-based power coefficient C_P^M is not an adequate objective function as its predictions deviate from empirical data by several orders of magnitude for larger m (figure 2a–e). On the other hand, due to the presence of muscle-consumed power, optimising power-consumption-based power coefficient C_P^T gives reasonable results (simi-

290 lar to optimising U or COT), suggesting that other reasonable measures could be at play in living

291 organisms.

292   The optimal motion envelopes $r(x)$ converge to fish-like motion envelopes, figure 3 (cf. $r(x)$

293 of initial population, figure S11). We show here $(r(x))_{U-opt}$ and $(r(x))_{COT-opt}$ for select m; the

294 envelopes within each optimal population $\Pi(m)$ and with the change in m vary smoothly between

295 those presented. Considering $(r(x))_{COT-opt}$, the motion is largely confined to the aft part of the

296 body which, together with $\lambda_b' = 1$, consistently resembles the (sub)carangiform motion [15, 20]

297 (the terminology is not uniform in the literature [27, 42]). Carangiform swimming has previously

298 been associated with low energetic costs [21]. Interestingly, a CFD study of mackerel and lamprey

299 swimming [8] found that at high Reynolds numbers, the (sub)carangiform motion is faster than

300 prescribed anguilliform motion. However, a direct comparison with our results (after matching Re

301 and λ_b/L) is not easy since a muscle model is not considered in [8] so it is not clear whether the

302 prescribed motion is physiologically feasible (see electronic supplementary material, section 4 for

303 details). Very small amplitudes of $(r(x))_{COT-opt}$ in $\mathcal{R}_T$ (cf. figure 2e) are in line with the decrease

304 in $(U)_{COT-opt}$. It is, however, possible that Lighthill's theory together with $C_D(Re)$ model provide

305 less accurate results in the boundary layer transition region $\mathcal{R}_T$. We note that in some cases, there

306 is significant motion of the head. This less-than-intuitive kinematics is a limitation of the present

307 body model wherein the muscle actuation extends throughout the fish body, including the head.

308   The changes in kinematic and energetic quantities across the scales and among performance

309 measures are accompanied by the shape modifications of optimal organisms, figure 4 (also figure

310 S12d-f). Relative to fish found in nature, the shapes show qualitative resemblances, for example,

311 the emergence of the caudal peduncle that is more pronounced for COT-optimal organisms in the

312 range $m = 1 \sim 100$ kg. Over the transition region $\mathcal{R}_T$ in the middle, optimal organisms have

313 generally smaller U and L than the allometric expectation as they try to remain in the laminar

314 regime. Such adaptations might be observed in nature with organisms that swim predominantly

315 near Re_{cr}. Although the shapes are mostly slender, lateral dimensions D and B reach $0.4L$ in

some cases (figure S12*e,f*), where Lighthill's theory may cease to be valid. Results corresponding to these shapes should be considered with care.

5. Discussion

This study shows, using relatively standard hydrodynamic and structural descriptions and a novel muscular model, how optimal undulatory swimming organisms might look and move if the driving force behind evolution were locomotory performance measures, in particular the swimming speed U and the cost of transport COT. If submodels of different complexity or different performance objectives are used, the overall optimisation framework should still be useful, although the detailed predictions would of course vary.

The body shape in nature primarily affects the hydrodynamics of swimming (in our model, it also influences the muscle performance through muscle disposition). The effect of shape on hydrodynamics in Lighthill's model is accounted for by the recoil equations (2), wherein the overall shape affects the total deflection $h(x, t)$. Lighthill's model exhibits limitations, however. The hydrodynamics at very long motion wave-lengths $\lambda_b \gg L$ is not correctly captured (see electronic supplementary material, section 4), therefore a constraint on the value of λ_b/L is required. The model also neglects vortex shedding, lateral flow separation, and viscous drag (relevant at lower Re numbers [13]). Despite these restrictions, Lighthill's model has been shown to provide sufficiently accurate values for the obtained lateral force [14, 43]. It is important to point out, however, that our primary interest is in the correct scaling of quantities with Re and the proper dependence on kinematic and geometric parameters, rather than in the quantitative accuracy (requiring substantially greater computational cost). For example, we have compared the scaling of the stride length with Re calculated by Lighthill's model and empirical drag formula with that from a more sophisticated hydrodynamic model [7]. Over the wide range of Re, the slopes of the predicted scaling agree to within $\sim 10\%$.

Modelling hydrodynamics with higher accuracy might be achieved at low Reynolds numbers Re ($O(10^3$–$10^4)$) where computational fluid dynamics (CFD) models solving the viscous flow equations [3, 7] are computationally feasible. However, the above Re-range covers only a small range of Re considered in this paper (which basically covers the entire range of fish and cetacean swimming). For such large Re numbers, potential flow models [6, 26, 43, 44] are often the only option. The large numbers of simulation evaluations required ($O(10^7)$ for this study) further limits the computationally feasible models to only the simplest ones. Lighthill's model provides a reasonable choice because it is valid for large Reynolds numbers Re and it is computationally very efficient.

Regardless of the complexity of the hydrodynamical model used, it alone cannot account for the losses that occur during the conversion of metabolic energy from food to useful mechanical work, nor can it assess the physiological feasibility of the prescribed motion, both of which are of a fundamental concern. For these reasons, the addition of muscle behaviour model is absolutely necessary if the overall swimming physics is to be considered.

We have introduced a novel muscle model primarily because the existing models for muscle behaviour during swimming do not provide the metabolic power consumption information [9–12]. Our model of muscle behaviour considers the contraction velocity $v(x,t)$ and the required contraction force $F_{musc}(x,t)$ as primary quantities, which avoids relying on still uncertain and variable relationship between F_{musc} and neural activity [15–17] as was done in previous studies [9–12]. The fact that the feasible combinations of the imposed motion $\hat{h}(x,t)$ and the required $F_{musc}(x,t)$ are determined by the available muscle and the intrinsic properties of muscle fibres is often overlooked in studies which only consider hydrodynamical aspect of swimming [3, 4, 7, 8].

Our results compare reasonably favourably across many scales, which lends validity to the present overall model, despite the assumptions and simplifications therein. None of the quantities presented in section 4 are *prescribed*; they are all outcomes of the optimisation procedure, i.e. our results give the values the optimal organisms would choose to employ. As such, our results are

fundamentally different from previous studies where a kinematic quantity (either Re [7,8] or neural activation [13, 14]) that directly sets the swimming speed was prescribed. We limit motion the wave-length to $\lambda_b/L = 1$, but that is a restriction on the degrees of freedom by which we describe the motion, not on a parameter that drives the motion. The value $\lambda_b/L = 1$ is roughly between those characteristic for the anguilliform and the carangiform swimming and is used by many fish species [15, 20, 27]. With such a choice, motion and geometry features of both swimming forms are found in optimal population Π. However, organisms with λ_b/L significantly different from 1, like lamprey or scup [15], or even "anguilliform mackerel" [8], cannot be correctly modelled with the present model. Relaxing the constraint on λ_b/L, which is undoubtedly an important parameter for swimming, would further enrich this study.

The lack of artificially imposed constraints enables us to obtain the intrinsic scaling of kinematic and energetic quantities as it emerges from the optimisation. Inherent allometric relationships (based on body mass m) are found for some quantities and they exhibit boundary layer regime dependence. Such scaling results have heretofore not been predicted from theoretical/numerical considerations alone. Discrepancies between the measured and predicted values might result from the likelihood that some measured values have not been obtained under the sustained swimming regime we assume, or that values of actual muscle and tissue properties differ from those we use. Improved predictions could presumably be achieved by tailoring the model parameters to a particular species (e.g. geometry, muscle properties and distribution); although uncertainty in measured data still remains, especially for larger m. Larger deviations might also indicate that other swimming or muscle behaviour not modelled here, or performance measures not presently considered, are involved.

Realistic overall results (figure 2–4) make it interesting to make a direct quantitative comparison between predicted shapes and kinematics of optimal organisms and select aquatic species over a range of m, figure 5. Despite the relative simplicity of the present model, including the low degrees-of-freedom in the modal representations of the shape and motion, we obtain a good

match. The conflicting nature of optimising COT and U contributes to the diversity of the obtained morphologies and behaviour. While parallels could be drawn between the performances of the real organisms and the theoretically predicted ones (e.g. the tuna-similar organism being close to COT-optimal — a feat for which tuna is often noted), the intent here is primarily to show that swimmers in real world do exhibit rather similar characteristics to those predicted. In spite of a possible bias in the selection of the specific examples, the overall corroboration of the model predictions by swimming animals in nature for diverse measures and across the scales is noteworthy.

While locomotion-based performance measures studied here are not necessarily the (only) important ones in nature, the present study provides a direct evidence of their impact on morphology. Comparisons of model-predicted morphological traits and those of real organisms also provide some means for deducing possible roles that specific performance measures might have played (causation) in the organisms' adaptation. A further insight into understanding the diversity of extant morphologies could be achieved by varying the choice of performance objectives and studying the predicted morphologies, based on the present optimisation framework. Understanding whether and how living morphologies are related to specific performance measures would also pave the way for improved biomimetic swimming vehicles.

Appendix A.

(a)   Assumed body/muscle/fluid properties

For simplicity, in all our calculations muscle and tissue properties are taken as length and size independent, but characteristic for fish (red fibre isometric force $F_0 = 150$ kN/m^2, $v_{max} = 5$ lengths/s [48], $E = 10^5$ N/m^2, $\nu_b = 10^4$ m^2/s [9, 14, 28], $\mu_0 = 0.1$ [25]). The standard metabolic rate used here is $P_s = 0.1327m^{0.80}$ [W] [49]. Fresh water properties are used throughout ($\rho = 10^3$

kg/m^3, $\nu = 10^{-6}$ m^2/s).

(b) Optimisation algorithm

The optimisation is conducted for organisms of mass $m = a10^b$, with $\log a = 0, 1/4, 1/2, 3/4$ and $b = -3, .., 6$. We use a multi-objective covariance matrix adaptation evolutionary strategy (MO-CMA-ES) [36], with default parameters. For every case, an initial randomly generated feasible population of 500 individuals is evolved through 500 generations. The optimisation converges in all cases, and the bounds imposed on the variables are never active in the final population.

(c) Shape similarity measure

We define the shape similarity measure $\mathcal{S}$ as

$$\mathcal{S} \equiv 1 - \int\limits_0^1 \frac{|d(x) - d_r(x)|}{\max(d_r(x))} \, dx \; .$$

It is bounded from above by 1, which marks a perfect similarity in shape. Here, x represents longitudinal coordinate normalised by the respective organism length L, such that both $d(x)$ and the height distribution of living organisms $d_r(x)$ (omitting fins and other appendages) are defined on $x \in [0, 1]$.

References

[1] Triantafyllou MS, Triantafyllou GS, Yue DKP. Hydrodynamics of fishlike swimming. Annu Rev Fluid Mech. 2000;32(1):33–53.

[2] Wu YT. Hydromechanics of swimming propulsion. Part 2. Some optimum shape problems. J Fluid Mech. 1971;46(03):521–544.

[3] Kern S, Koumoutsakos P. Simulations of optimized anguilliform swimming. J Exp Biol. 2006;209(24):4841–4857.

[4] Eloy C, Schouveiler L. Optimisation of two-dimensional undulatory swimming at high Reynolds number. International Journal of Non-Linear Mechanics. 2011 May;46(4):568–576.

[5] Kagemoto H, Yue DKP, Triantafyllou M. Optimization of a fish-like swimming body. In: American Physical Society, Division of Fluid Dynamics Meeting; 1997. .

[6] Zhu Q, Wolfgang MJ, Yue DKP, Triantafyllou MS. Three-dimensional flow structures and vorticity control in fish-like swimming. J Fluid Mech. 2002;468(-1):1–28.

[7] Borazjani I, Sotiropoulos F. Numerical investigation of the hydrodynamics of carangiform swimming in the transitional and inertial flow regimes. J Exp Biol. 2008;211(10):1541–1558.

[8] Borazjani I, Sotiropoulos F. On the role of form and kinematics on the hydrodynamics of self-propelled body/caudal fin swimming. J Exp Biol. 2010 Jan;213(1):89–107.

[9] Long J. Force transmission via axial tendons in undulating fish: a dynamic analysis. Comp Biochem Physiol A. 2002;133(4):911–929.

[10] van Leeuwen JL, Lankheet MJM, Akster HA, Osse JWM. Function of red axial muscles of carp (Cyprinus carpio): recruitment and normalized power output during swimming in different modes. J Zool. 1990;220(1):123–145.

[11] Williams TL. A new model for force generation by skeletal muscle, incorporating work-dependent deactivation. J Exp Biol. 2010 Feb;213(4):643–650.

[12] Jordan CE. Coupling internal and external mechanics to predict swimming behavior: a general approach. Amer Zool. 1996;36(6):710–722.

[13] McMillen T, Williams T, Holmes P. Nonlinear muscles, passive viscoelasticity and body taper conspire to create neuromechanical phase lags in anguilliform swimmers. PLoS Comput Biol. 2008 Aug;4(8):e1000157+.

[14] Tytell ED, Hsu CY, Williams TL, Cohen AH, Fauci LJ. Interactions between internal forces, body stiffness, and fluid environment in a neuromechanical model of lamprey swimming. PNAS. 2010 Nov;107(46):19832–19837.

[15] Wardle C, Videler J, Altringham J. Tuning in to fish swimming waves: body form, swimming mode and muscle function. J Exp Biol. 1995;198(8):1629–1636.

[16] Coughlin DJ. Aerobic muscle function during steady swimming in fish. Fish Fish. 2002;3(2):63–78.

[17] Syme DA, Gollock M, Freeman MJ, Gamperl KA. Power isn't everything: Muscle function and energetic costs during steady swimming in Atlantic Cod (Gadus morhua). Physiol Biochem Zool. 2008;81(3):320–335.

[18] Lighthill MJ. Hydromechanics of aquatic animal propulsion. Annu Rev Fluid Mech. 1969;1(1):413–446.

[19] Webb PW. Body form, locomotion and foraging in aquatic vertebrates. Am Zool. 1984 Jan;24(1):107–120.

[20] Videler JJ. Fish Swimming. Chapman & Hall, London; 1993.

[21] Webb PW. Exercise performance of fish. In: Advances in veterinary science and comparative medicine. vol. 38B. Academic Press; 1994. p. 1–49.

[22] Walker JA, Ghalambor CK, Griset OL, Mckenney D, Reznick DN. Do faster starts increase the probability of evading predators? Functional Ecology. 2005;19(5):808–815.

[23] Langerhans RB. Trade-off between steady and unsteady swimming underlies predator-driven divergence in Gambusia affinis. Journal of Evolutionary Biology. 2009;22(5):1057–1075.

[24] Rome LC, Swank D, Corda D. How fish power swimming. Science. 1993;261(5119):340–343.

[25] Syme DA. Functional properties of skeletal muscles. In: Shadwick RE, Lauder GV, editors. Fish Biomechanics: Fish Physiology. vol. 23. Academic Press, New York; 2006. p. 179–240.

[26] Lighthill MJ. Note on the swimming of slender fish. J Fluid Mech. 1960;9(02):305–317.

[27] Webb PW. Hydrodynamics and energetics of fish propulsion. Dept. of the Environment Fisheries and Marine Service; 1975.

[28] Cheng JY, Pedley TJ, Altringham JD. A continuous dynamic beam model for swimming fish. Philos Trans R Soc London, Ser B. 1998;353:981–997.

[29] Jayne B, Lauder G. Are muscle fibers within fish myotomes activated synchronously? Patterns of recruitment within deep myomeric musculature during swimming in largemouth bass. J Exp Biol. 1995;198(3):805–815.

[30] Jayne B, Lauder G. Red muscle motor patterns during steady swimming in largemouth bass: effects of speed and correlations with axial kinematics. J Exp Biol. 1995 July;198(7):1575–1587.

[31] Alexander MR. Optimum muscle design for oscillatory movements. J Theor Biol. 1997;184(3):253–259.

[32] Shadwick RE, Katz SL, Korsmeyer KE, Knower T, Covell JW. Muscle dynamics in skipjack tuna: timing of red muscle shortening in relation to activation and body curvature during steady swimming. J Exp Biol. 1999;202(16):2139–2150.

[33] Schultz W, Webb PW. Power requirements of swimming: Do new methods resolve old questions? Integr Comp Biol. 2002;42(5):1018–1025.

[34] Wu TY. Introduction to the scaling of aquatic animal locomotion. In: Pedley TJ, editor. Scale Effects in Animal Locomotion. New York: Academic Press; 1977. p. 203–232.

[35] Deb K. Multi-objective optimization using evolutionary algorithms. Wiley, New York; 2001.

[36] Igel C, Hansen N, Roth S. Covariance matrix adaptation for multi-objective optimization. Evol Comput. 2007;15(1):1–28.

[37] Block BA, Booth D, Carey FG. Direct measurement of swimming speeds and depth of blue marlin. J Exp Biol. 1992;166(1):267–284.

[38] American Cetacean Society Fact Sheet. http://www.acsonline.org/factpack/bluewhl.htm; 2010.

[39] Yates GT. Hydromechanics of body and caudal fin propulsion. In: Webb PW, Weihs D, editors. Fish Biomechanics. New York: Praeger Publishers; 1983. p. 177–213.

[40] Askew GN, Marsh RL. Optimal shortening velocity (V/Vmax) of skeletal muscle during cyclical contractions: length-force effects and velocity-dependent activation and deactivation. J Exp Biol. 1998;201(10):1527–1540.

[41] van Leeuwen JL. The action of muscles in swimming fish. Exp Physiol. 1995;80:177–191.

[42] Lauder GV, Tytell ED. Hydrodynamics of undulatory propulsion. In: Shadwick RE, Lauder GV, editors. Fish Biomechanics: Fish Physiology. vol. 23. Academic Press, New York; 2006. p. 425–468.

[43] Kagemoto H, Wolfgang MJ, Yue DKP, Triantafyllou MS. Force and power estimation in fish-like locomotion using a vortex-lattice method. J Fluids Eng. 2000;122(2):239–253.

[44] Wu TYT. Hydrodynamics of swimming of fish and cetaceans. In: Yih CS, editor. Advances in Applied Mechanics. vol. 11. Academic Press, New York; 1971. p. 1–63.

[45] Wardle C, Videler J, Arimoto T, Franco J, He P. The muscle twitch and the maximum swimming speed of giant bluefin tuna, Thunnus Thynnus L. J Fish Biol. 1989 JUL;35(1):129–137.

[46] Rohr JJ, Fish FE. Strouhal numbers and optimization of swimming by odontocete cetaceans. J Exp Biol. 2004;207(10):1633–1642.

[47] Search FishBase. http://www.fishbase.org; 2010.

[48] Medler S. Comparative trends in shortening velocity and force production in skeletal muscles. Am J Physiol-Reg I. 2002;283(2):R368–R378.

[49] Clarke A, Johnston NM. Scaling of metabolic rate with body mass and temperature in teleost fish. J Anim Ecol. 1999;68(5):893–905.
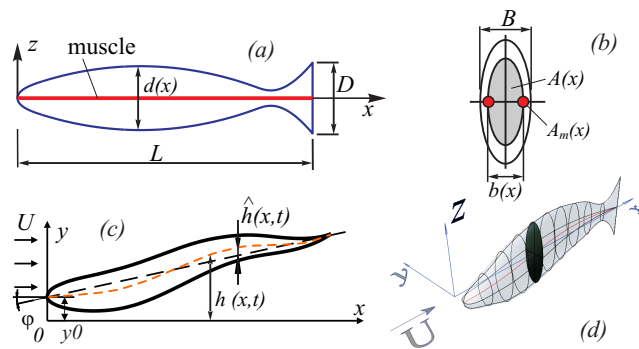
Figure 1: Description of body shape and motion. (*a*) Lateral view of an organism of arbitrary shape and idealised muscle layout (red line). (*b*) Body cross-section of area $A(x)$ and muscle cross-section of area $A_m(x)$ on each side of the body (red). (*c*) Dorsal view of the motion kinematics. (*d*) Three-dimensional view of a body with a cross-section highlighted.
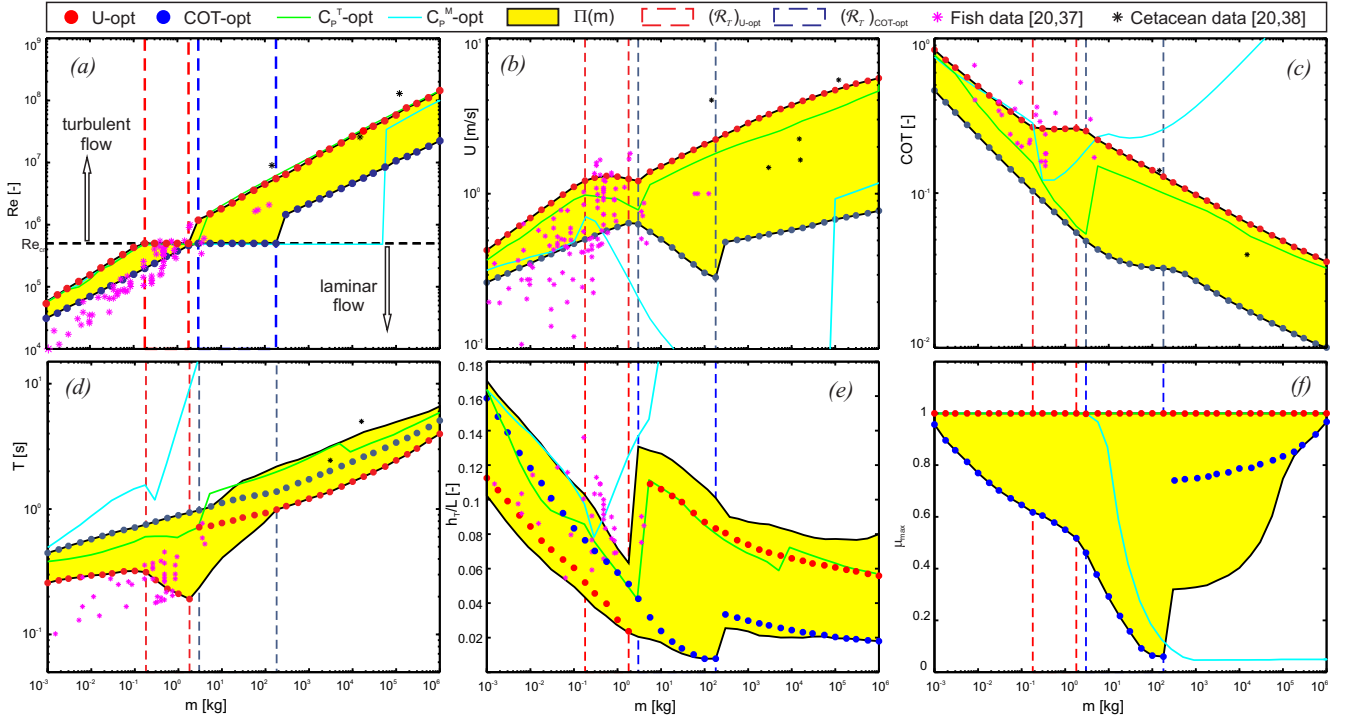
Figure 2: Swimming characteristics of optimal populations $\Pi(m)$ compared to empirical data for fish [20, 37] (magenta stars) and cetaceans [20, 38] (black stars). Organisms with minimum COT are marked by blue circles and U-optimal organisms by red circles; the rest of $\Pi(m)$ are represented by yellow region(s). The transition region $(\mathcal{R}_T)_{U-opt}$ is marked by red dashed line and $(\mathcal{R}_T)_{COT-opt}$ by blue dashed line. Alternative objective functions, power-output-based power coefficient C_P^M (cyan line) and total-power-based power coefficient C_P^T (green line), are also shown for comparison. Where mass measurements are missing, they are obtained from an $m - L$ allometric expression ($m = 12.62L^{3.11}$). (a) Reynolds number Re. (b) Sustained swimming speed U. (c) Cost of transport COT. (d) Tail beat period T. (e) Relative tail amplitude h_T/L. (f) Maximum active muscle portion μ_{max}.

Figure 3: Motion envelopes $r(x)$ of optimal organisms for select m. $(r(x))_{COT-opt}$ is denoted by blue, and $(r(x))_{U-opt}$ by red lines. Axes are not to scale.
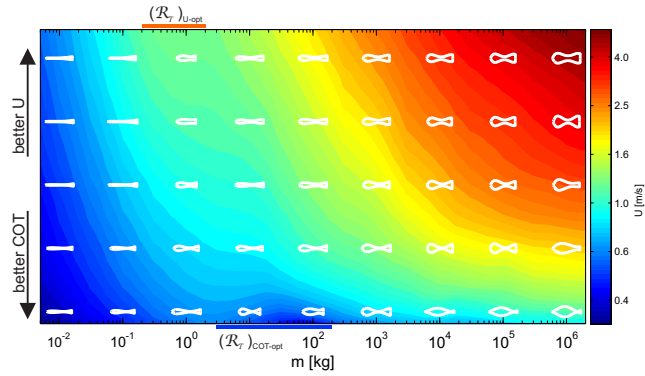
Figure 4: Representative shapes from optimal populations Π, rank-ordered from optimal COT to optimal U, with corresponding values of attained U as colour contours. The body shapes are scaled by the expected allometric length, $L = 0.443m^{0.321}$, based on organisms of mass m.
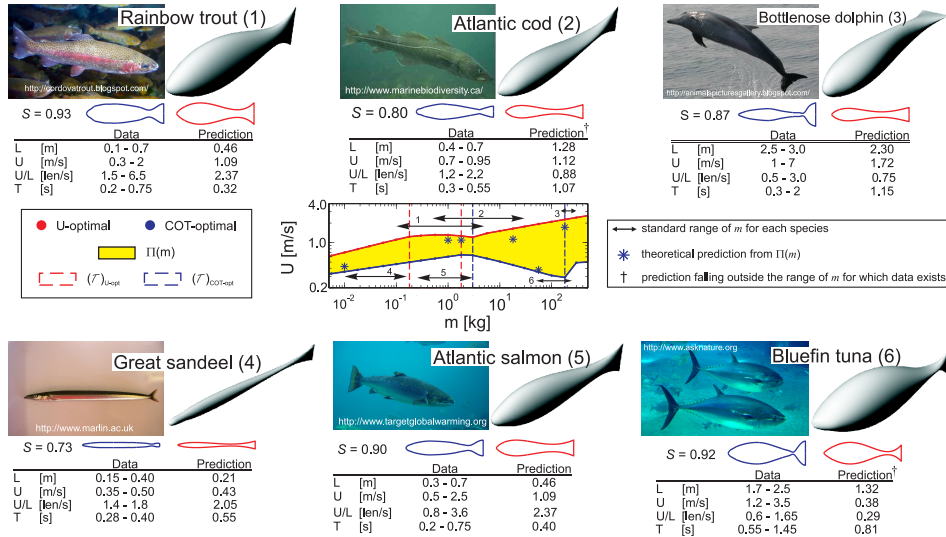

Figure 5: Comparisons of shape and swimming characteristics between model predictions and representative fish and cetacean species [20, 45–47]. In each example, from optimal populations $\Pi(m)$ that cover the species' standard range of m (double arrowhead line), an organism ($*$) is selected that best matches kinematic data and shape for that species. The predictions falling notably outside the range of m for which kinematic data exists are denoted by $\dagger$. Three-dimensional shapes of theoretically predicted organisms are depicted alongside photographs of real swimmers for qualitative comparison. The body shapes of each species are outlined neglecting the fins and the trailing profile of the tail (blue line) and quantitatively compared with the predicted shapes (red line) using the shape similarity measure $\mathcal{S}$ (see Appendix).

Electronic Supplementary Material:
Optimal Shape and Motion of Undulatory Swimming Organisms

Grgur Tokić,[1] Dick K.P. Yue[1]

[1]Department of Mechanical Engineering, Massachusetts Institute of Technology,
Cambridge, MA 02139, USA

1   Methods

1.1   Shape representation

The hydrodynamical model [1] used here does not model flow separation. The flow separation due to abrupt changes in body shape leads to increased drag which, thus, would not be recorded using the present hydrodynamical model and would not be penalized during the optimisation procedure.

In order to prevent too abrupt changes, we seek to describe the shape in a sufficiently smooth way such that a possibility for non-physical changes in shape, which would certainly be smoothed out in reality, is minimal. We require the shape to have a smooth snout at $x = 0$ and a finite height at $x = L$. The parametrisation presented in (9) satisfies these requirements—the rounded nose and the finite tail height are achieved by $\sqrt{x}$; the Chebyshev-based polynomial shape functions D_n add variety to the shape. This parametrisation also avoids a possible singularity at $x = 0$ for the calculation of hydrodynamical force F_L.

The expansion (9) converges rapidly, requiring only $N_S = 3 \sim 4$ to achieve relative errors of 3% or less for fish-like bodies, Fig. S2. The optimisation is conducted with the first three D_n ($N_S = 2$) to allow for the flexibility in the possible shapes, but to prevent oscillations which could hardly be damped out by the hydrodynamical model used.

Width of the body $b(x)$ is defined as a symmetrical NACA - 00 profile given by:

$$\frac{b(x)}{L} = \frac{B/L}{0.1}\left(0.2969\sqrt{x} - 0.1260x - 0.3516x^2 + \right.$$
$$\left. +0.2843x^3 - 0.1015x^4 - 0.0021x\right)$$

where the last term has been added to ensure zero thickness at the tail. The thickness B/L is one of the parameters being optimised.
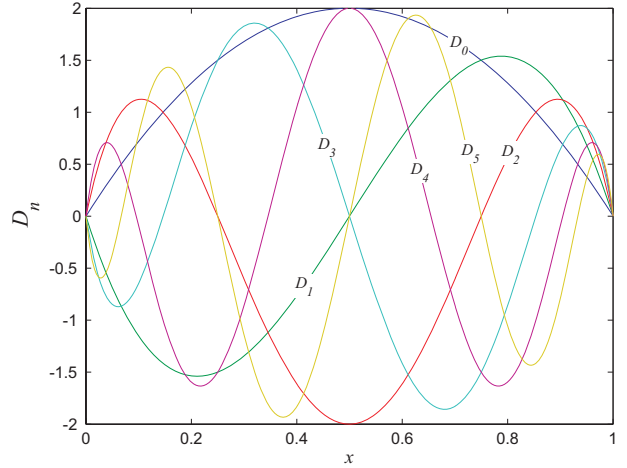

Figure S1: First 6 modes of shape functions $D_n(x)$

In total, we parametrise the shape of the body by five parameters: $B/L, D/L, C_0, C_1, C_2$.

1.2   Motion representation

The motion envelope $r(x)$ is parametrised in terms of Chebyshev series for the purpose of optimisation. Only the first three terms of the series have been used to define $r(x)$ as that gives wide enough flexibility to the envelope shape and keeps the number of optimisation variables low. Thus, $\hat{h}(x,t)$ can be written as

$$\hat{h}(x,t) = \sum_{n=0}^{2}{}' R'_n T_n(x) \cos(2\pi x/\lambda_b - \omega t) \qquad \text{(S.1)}$$

where λ_b is the length of body-motion undulation.

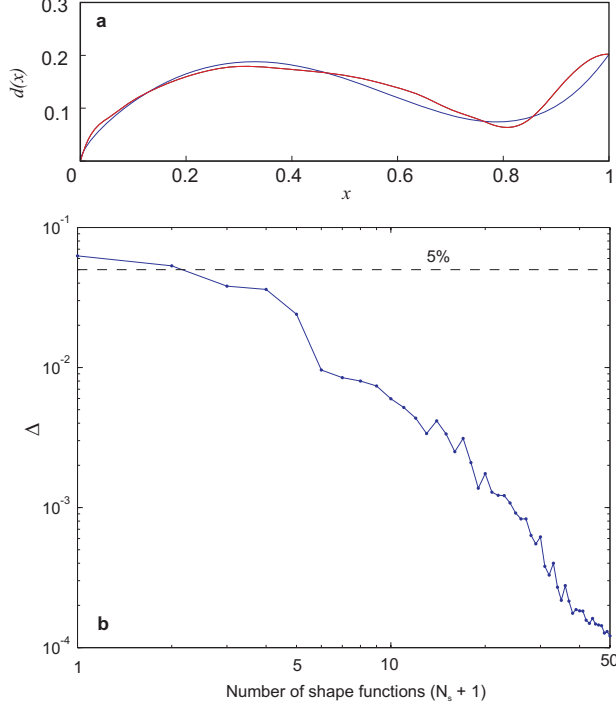The parametrisation of $r(x)$ is in fact implemented such

Figure S2: Convergence to the prescribed shape with the number of basis functions N_S. Here shown for Atlantic salmon *Salmo salar*. *(a)* Prescribed shape (red line) and its approximation (blue line) using $N_S = 2$. *(b)* Relative deviation from the given shape Δ as a function of total number of shape basis functions D_n.

that it is written as

$$r(x) = \hat{h}_T \sum_{n=0}^{2}{}' R_n T_n(x), \quad (S.2)$$

with the requirement that $\sum_{n=0}^{2}{}' R_n = 1$, giving the tail amplitude to be $\hat{h}_T$. The motion envelope optimisation variables are then $\hat{h}_T$, R_0 and R_1, which are easier to bound than three R'_n Chebyshev coefficients would be.
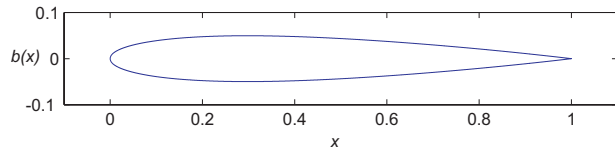
In total, the motion is parametrised using four optimi-

Figure S3: An example of the width profile $b(x)$ (NACA-0010)

sation variables: Re, $\hat{h}_T$, R_0 and R_1. A large variety of admissible motion envelopes, Fig. S11, together with a range of possible Re and $\hat{h}_T$ values, accounts for the diversity of obtainable motion patterns.

1.2.1 The treatment of boundary conditions

Since we assume a small lateral recoil, the condition (4) on $h(x,t)$ transforms to the same conditions on $\hat{h}(x,t)$. In general, for arbitrarily selected $r(x)$ and λ_b, (4) will not be satisfied so $\hat{h}(x,t)$ has to be corrected.

We calculate the correction by converting $\hat{h}(x,t)$ into the Fourier-Chebyshev expansion

$$\hat{h}(x,t) = \sum_{m=-1}^{1} \sum_{n=0}^{N}{}' A_{mn} T_n(x) e^{im\omega t}, \quad (S.3)$$

where A_{mn} are the complex coefficients accounting for the spatial distribution of motion envelope $r(x)$ and phase function $2\pi x/\lambda_b$. N can be arbitrarily large; we set $N = 50$ which makes the residual between (S.1) and (S.3) negligible. Note that there is no mean displacement $A_{0,n} \equiv 0$; and that $A_{-1,n}$, $A_{1,n}$ are complex conjugate pairs so only $A_{1,n}$ has to be calculated.

With (S.3), (4) becomes

$$\sum_{n=0}^{N}{}' A_{1,n} \left.\frac{d^2 T_n}{dx^2}\right|_{x=0,1} = \delta_{0,1} ,$$
$$\sum_{n=0}^{N}{}' A_{1,n} \left.\frac{d^3 T_n}{dx^3}\right|_{x=0,1} = \delta'_{0,1} . \quad (S.4)$$

The residuals $\delta_{0,1}$ and $\delta'_{0,1}$ are in general non-zero and should be corrected for. Generally, (S.4) could be satisfied by modifying $A_{1,N-3},\ldots,A_{1,N}$, making the contribution of the last four terms in the expansion of $\hat{h}(x,t)$ non-negligible even at the second derivative. However, that causes global oscillations in the calculations of higher derivatives of $h(x,t)$ (derivatives up to the fourth are used in the calculation of the required bending moment (3)), and the lack of convergence with increase an in N.

In order to satisfy (4) and prevent unwanted global oscillation of $\hat{h}(x,t)$, we add a corrective function $\delta(x)$ to the second derivative of the original motion, such that it accounts for the non-zero boundary conditions (S.4) at the ends but drops down to zero everywhere else exponentially fast. We write $\delta(x)$ as

$$\delta(x) = (\delta_0 + (\delta'_0 + \alpha\delta_0) x) e^{-\alpha x} +$$
$$+ (\delta_1 + (\delta'_1 - \alpha\delta_1)(x-1)) e^{\alpha(x-1)} \quad (S.5)$$
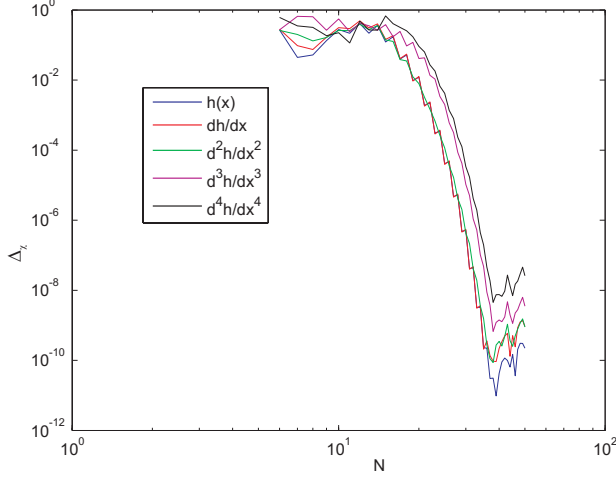
Figure S4: Convergence of the corrected motion representation with the order of Chebyshev expansion N. The relative difference is defined as $\Delta_\chi \equiv (\max \chi^N - \max \chi^{N-1})/\max \chi^N$, where χ is $\hat{h}$ from (S.8) or one of its first four derivatives.

where the parameter α is set to be $\alpha = 35$. The function $\delta(x)$ is then represented in Chebyshev series up to the order N,

$$\delta(x) = \sum_{n=0}^{N}{}' C_n^\delta T_n(x) \tag{S.6}$$

with the imposed boundary conditions

$$\delta(x = 0, 1) = \delta_{0,1}; \quad \left.\frac{d\delta}{dx}\right|_{x=0,1} = \delta'_{0,1} \tag{S.7}$$

The boundary conditions (S.7) are satisfied by modifying $C_{N-3}^\delta, \ldots, C_N^\delta$. After correction, $\delta(x)$ is integrated twice [2] to yield new corrected coefficients $C_n^{\delta,corr}$. These are then subtracted from $A_{1,n}$, giving the new corrected coefficients for $\hat{h}(x, t)$

$$A_{1,n}^{corr} = A_{1,n} - C_n^{\delta,corr}.$$

$$\hat{h}(x, t) = \sum_{m=-1}^{1} \sum_{n=0}^{N}{}' A_{mn}^{corr} T_n(x) e^{im\omega t}, \tag{S.8}$$

With this correction, most of the original motion is not polluted by high harmonics and the convergence with the increase in spectral harmonics N is exponentially fast, Fig. S4. Hence, once the motion parameters at each step of optimisation process have been defined, all the subsequent calculations are performed with $\hat{h}(x, t)$ expressed by (S.8).
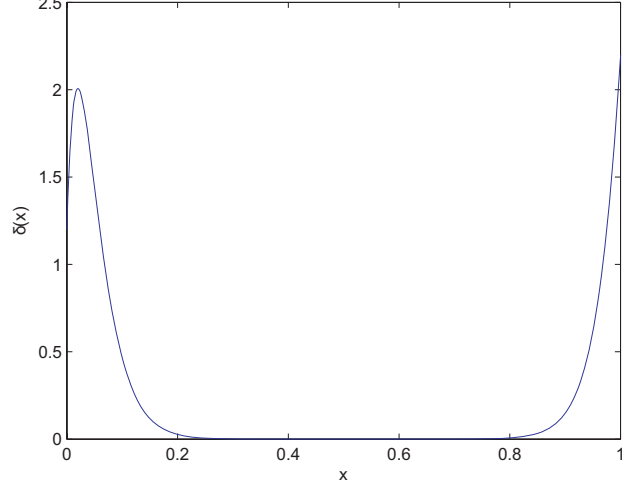

Figure S5: Corrective function $\delta(x)$ for $\delta_0 = 1.2$, $\delta_1 = 2.2$, $\delta'_0 = 100$, $\delta'_1 = 50$ and $\alpha = 35$.

1.2.2 Recoil calculation

For U and $\hat{h}(x, t)$ given, we obtain the unknown recoil functions $y_0(t)$ and $\phi(t)$ by expressing them in the form of Fourier series

$$y_0(t) = \Re e \left(\sum_{m=-M}^{M} Y_m e^{im\omega t} \right),$$

$$\phi(t) = \Re e \left(\sum_{m=-M}^{M} \Phi_m e^{im\omega t} \right)$$

where Y_m and Φ_m are the complex coefficients which need to be determined from (2). Analogously to A_{mn}, Y_m and Φ_m come in complex conjugate pairs and $Y_0, \Phi_0 \equiv 0$, so only the calculation of Y_1 and Φ_1 is required for $M = 1$. It can be shown that Y_1 and Φ_1 are the solutions of a 2-by-2 system

$$FV + Y_1 FT + \Phi_1 FR = 0$$
$$MV + Y_1 MT + \Phi_1 MR = 0$$

or, written in matrix form,

$$\begin{bmatrix} FT & FR \\ MT & MR \end{bmatrix} \begin{Bmatrix} Y_1 \\ \Phi_1 \end{Bmatrix} = - \begin{Bmatrix} FV \\ MV \end{Bmatrix}. \tag{S.9}$$

The complex coefficients FT, FR, FV, MT, MR, MV are known and depend on the body geometry, A_{mn}, U and ω. The system (S.9) is solved to obtain Y_1 and Φ_1 for every imposed motion $\hat{h}(x, t)$ and shape during the optimisation process.
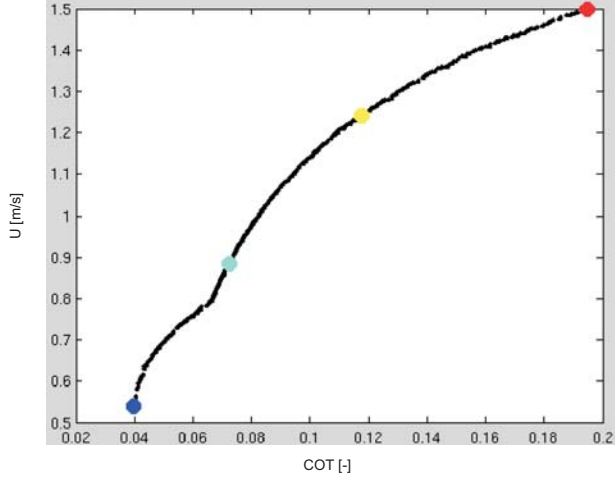
Figure S6: An example of non-convex Pareto front for a final population in $(\mathcal{R}_T)_{COT-opt}$. The kink can cause more abrupt changes in the characteristics of optimal organisms on **P**

1.3 Optimisation setup

Evolutionary optimisation algorithms work with populations of individuals (representing different solutions) which are evolved through generations using some adaptation criteria to obtain better objective function values. The complexity of the objective space poses little problems to the evolutionary algorithms since they do not require gradient information so they are well suited for non-linear, non-convex, non-smooth problems. Since there is always a probability to sample the space away from the current minimum, evolutionary methods are more capable of reaching the global optimum than gradient-based methods, which would have additional problems with non-smooth problems (as the present one is).

A useful way of representing the optimal population Π for two-objective problems is by a Pareto front in the two-dimensional objective space [3]. The Pareto front is made out of non-dominated solutions only and it illustrates the functional trade-offs between the conflicting objectives. A big advantage evolutionary optimisation methods have when dealing with multi-objective problems is in their inherent ability to reach the Pareto front in one run, without additional *a priori* information, since the entire population is advanced at once [3]. Evolving entire populations makes possible non-convexity of the Pareto front amendable to the evolutionary optimisation methods.

Since swimming is a non-linear, possibly non-convex (Fig. S6) and a non-smooth problem, we use state-of-the-art evolutionary optimisation algorithm—multi-objective

covariance matrix adaptation evolutionary strategy MO-CMA-ES [4]. MO-CMA-ES has excellent performance in converging to the final solution in terms of required function evaluations (smaller population sizes, number of generations), compared to some other evolutionary algorithms. This fact has been already reported [4] and confirmed by our tests.

The optimisation is conducted for organisms of mass $m = a10^b$, with $\log a = 0, 1/4, 1/2, 3/4$ and $b = -3, .., 6$. Default parameters for MO-CMA-ES have been used, with population size $n_{pop} = 500$ and 500 generations. There is a total of $N_p = 9$ optimisation variables $\xi \equiv [Re, \hat{h}_T, R_0, R_1, D/L, B/L, C_0, C_1, C_2]$. Box constraints (i.e. upper and lower bounds) are set on optimisation variables to reduce the variable space that needs to be explored, with the exception that for Re the bounds are set on $\log(Re)$. This prevents the large deformation of variable space in Re-direction which would otherwise happen since Re can have many order-of-magnitude changes during the optimisation. The initial random population explores the parameter space, while the final populations were not influenced by the bounds we set, i.e. all the solutions are found within the bounds, Fig. S7.
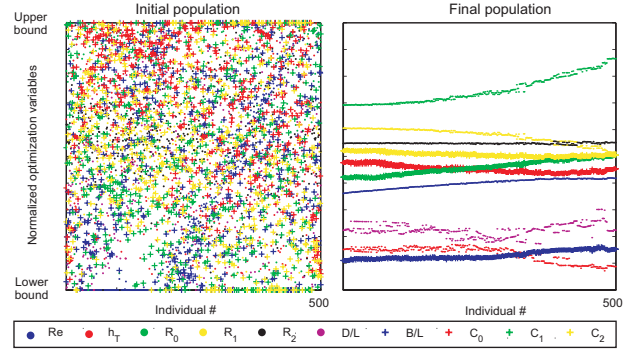

Figure S7: Normalised optimisation variables of the initial and final generation. The normalised optimisation variables are defined as $\xi_n = (\xi - \xi_{lb})/(\xi_{ub} - \xi_{lb})$, where ξ_{lb} and ξ_{ub} are lower and upper bounds imposed on optimisation variables, respectively.

In addition to the physical motion feasibility conditions (7) and the box constraints set on optimisation variables, motion and shape integrity conditions due to parametrisation require

$$r(x) > 0$$
$$d(x) \geq d_0(x) \qquad \text{(S.10)}$$
$$d_0(x) = 0.025D(1 - e^{-20x/L})$$

where $d_0(x)$ accounts for minimal height (set to $\sim$

0.025D here) the organism has to have, ensuring structural integrity. This was, in some cases, an active constraint for the maximal reduction in the caudal peduncle area.

Initial generation is required to be feasible (i.e. (S.10), (7) satisfied for all individuals) and it is randomly chosen. The feasibility of initial population improves the performance of the optimisation algorithm which would otherwise be often trapped in non-physical areas of variable space. Optimisation variables' values for the later generations are randomly chosen such that they always satisfy (S.10), and we leave to the optimisation algorithm to find the individuals that satisfy (7) as well.

CMA-ES algorithm cannot satisfy hard box constraints on optimisation variables (there is always some probability, albeit very small, that the randomly chosen individual will fall out of these bounds), so the deviation outside the bounds is penalized by a weighted square of the distance to the bounds. The penalisation for not satisfying inequality constraints (e.g. (7)) is problem specific, and we treat it by adding/subtracting an exponentially growing function $e(\Delta c) = \exp(10|\Delta c|) - 1$ to/from the objective function, depending whether it is being minimized/maximized. Here, $|\Delta c|$ is the maximum constraint violation. This penalisation has proved to have satisfactory performance and the individuals remain in the feasible region throughout the optimisation, after the adjustments in few initial generations.

In order to have equally scaled objective space and, thus, possibly improving the performance of the optimisation algorithm, the optimisation objectives COT and U were normalised by their expected values from empirical scaling laws [5]

$$\widetilde{COT} = \frac{COT}{0.33m^{-0.24}}; \quad \widetilde{U} = \frac{U}{0.50m^{0.27}};$$

the optimisation is then conducted over $\widetilde{COT}$ and $\widetilde{U}$. This scaling does not influence the results of the optimisation since the optimisation is conducted for known m.

1.3.1 Convergence tests and sensitivity analysis

We use standard parameter settings for MO-CMA-ES [4], with population size $n_{pop} = 500$ and number of generations $n_{gen} = 500$. Convergence tests have been done for several different masses m, with respect to population size n_{pop} and number of generations n_{gen}. MO-CMA-ES does not require population sizes as large as some other multi-objective optimisation methods, and $n_{pop} = 500$ has proved to be an adequate population size to allow for the convergence to a consistent Pareto front. For a given

n_{pop}, n_{gen} is chosen such that the individuals have converged to a Pareto front (figure S8).
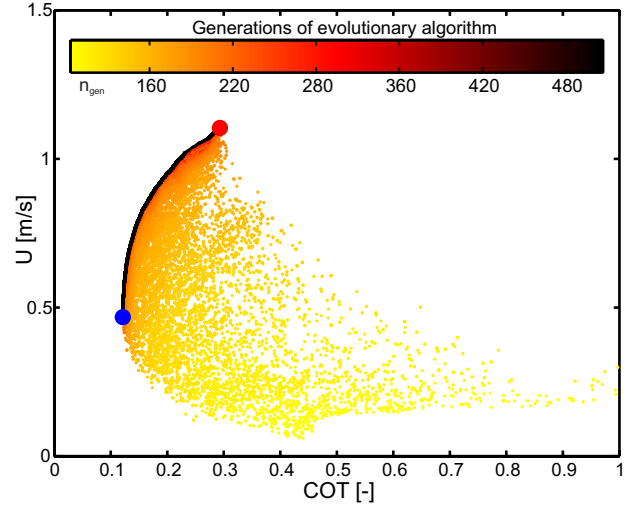

Figure S8: Pareto front convergence. The colourmap indicates different generations n_{gen} as the population converges to the final solution (from $n_{gen} = 100$ to $n_{gen} = 500$). The final Pareto front is depicted in black.

To ensure that the final Pareto front is a global one, many runs with different random number seeds are conducted, and the combined non-dominated front from all these runs is considered as the final Pareto front. Since we are performing the optimisation for a sequence of increasing m, the smooth transition of $(\cdot)_{COT-opt}$ and $(\cdot)_{U-opt}$ values with the increase in m serves as an additional indication that the global Pareto front has been reached.

Two additional comparisons are made to ensure that final solution has in fact the fully converged. We have compared the results obtained by MO-CMA-ES to the results obtained by single-objective covariance matrix adaptation evolutionary strategy (CMA-ES) [6, 7], running it separately for COT and U optimisation. This allowed us to compare the $(\cdot)_{COT-opt}$ and $(\cdot)_{U-opt}$ values obtained by the two methods. The comparison shows no difference in results between the two methods.

We have also made a comparison with the results obtained using a different multi-objective evolutionary algorithm, NSGA-II [8]. Standard settings were used for NSGA-II. The results obtained by this method mostly match those obtained by MO-CMA-ES, but the method suffers from being stuck on local Pareto fronts, making non-smooth transitions between solutions for different m. It also requires large number of generations and large population sizes for convergence ($n_{pop} = 10000$, $n_{gen} = 500$), making the use of the method prohibitive.

Sensitivity analysis was also performed, where only some optimisation variables were included in the optimisation, and the results were shown to be robust. In these cases, the values of U and COT are slightly sub-optimal, compared to the values presented in this paper where all the variables were optimised at once.

2 Drag coefficient

The drag coefficient C_D around a swimming body can be modelled as the friction coefficient of a flat plate C_f corrected for thickness effects [9], giving

$$C_D = C_f(1 + 1.5D_L^{1.5} + 7.0D_L^3)$$

$$C_f = \begin{cases} 1.33\,Re^{-0.5}, & Re < 5.0 \cdot 10^5 \\ 0.072\,Re^{-0.2}, & Re > 5.0 \cdot 10^5 \end{cases} \quad \text{(S.11)}$$

where D_L denotes the maximum lateral dimension of the body normalised by body length L. This relation shows a discrete jump when transitioning from laminar to turbulent regime at $Re = 5.0 \cdot 10^5$, figure S9.
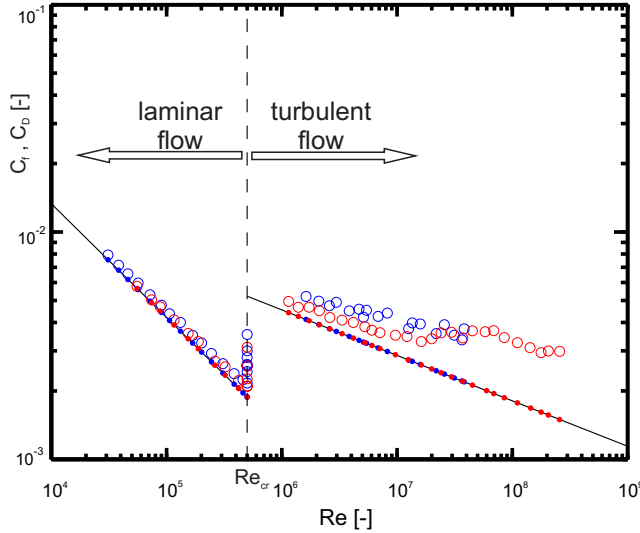

Figure S9: Drag coefficient C_D and friction coefficient C_f. The solid line represents the C_f–Re relationship (S.11). The obtained C_f (solid circles) and C_D (empty circles) of optimal organisms is denoted by in red/blue color for U- and COT-optimal organisms, respectively.

3 Muscle model details

3.1 Continuity assumptions

Along with the assumptions made in the main text, we make further assumptions on the geometrical and morphological characteristics of muscles. The muscle fibres forming the muscle are organised into myotomes and can be contracted segmentally along the length [10]. We assume the myotome length to be infinitesimally small to enable a continuous length-wise representation of F_{musc} (myotome lengths in real fish have been reported to be $\approx 0.005L$ [11]). Since any muscle cross-section is of much smaller area than the corresponding body cross-section ($\mu_0 \ll 1$) and since it is located far away from the neutral axis ($\sqrt{A_m(x)} \ll b(x)/2$), the contraction velocity v is assumed to be uniform over any muscle cross-section. The muscle is longitudinally and laterally heavily innervated [10] to allow different muscle employment patterns.

3.2 Hill's muscle model

We assume that muscle fibres operate on the plateau of length-tension curve at all times during steady swimming [12] so the effect of the fibre excursion on the contraction force can be neglected.

Hill's constitutive relation between contractive force F_{fib} a muscle fibre exerts during steady isotonic contraction and the contraction velocity v is given by [13]:

$$F_{fib} = F_0 \begin{cases} 1.8 - 0.8\dfrac{1 + v_r}{1 - 7.56Gv_r}, & -1 \leq v_r < 0 \\ \dfrac{1 - v_r}{1 + Gv_r}, & 0 \leq v_r \leq 1 \end{cases} \quad \text{(S.12)}$$

where we have taken $G = 4$, following [13]. The metabolic power P_{fib} consumed by the fibre is,

$$P_{fib}/F_0 v_{max} = \begin{cases} 0.01 - 0.11v_r + 0.06\exp(23v_r), \\ 0.23 - 0.16\exp(-8v_r), \end{cases} \quad \text{(S.13)}$$

for $-1 \leq v_r < 0$ and $0 \leq v_r \leq 1$, respectively.

3.3 The validity of our muscle model

The assumptions behind our muscle model have been repeatedly validated in the literature. However, it is interesting to compare the final predictions of the overall muscle model with empirically measured data, in the absence of hydrodynamical and structural models, to make sure that the assumptions do not conflict against each other.

The obtainable values of contractive force $F(x,t)$ and contraction velocity $v(x,t)$ are directly governed by the chosen (realistic) values of F_0 and v_{max} and, hence, are realistic. However, secondary quantities which characterise the time-averaged muscle behaviour provide a stricter test.

To isolate the effect of muscle model alone from the effects caused by different muscle employment patterns, we compare the maximum achievable local muscle efficiency $\eta_{M'}$ with the empirical measurements. The local muscle efficiency at some cross-section x is defined as

$$\eta_{M'}(x) \equiv \overline{P_{mech}}(x)/\overline{P_{musc}}(x).$$

Based on our model, $\eta_{M'}$ can achieve a maximum value of 44.6%, which is comparable to empirically obtained maximum efficiency of red muscle fibers of 51% [14].

The efficiency of isolated muscle fibres is greater than the overall muscle efficiency in swimming organisms. This total muscle efficiency is found to be around 20% in real fish [9, 15]. Our theoretically predicted organisms obtain muscle efficiencies of 3%–20%, depending on the size and the location on the Pareto front.

4   Validity of Lighthill's theory

Lighthill's slender body theory [1] is valid for slender body geometry and small lateral motion. While most of the shapes of optimal population Π can be considered slender, some of the shapes in the initial population cannot be considered as such due to abrupt changes in geometry (figure S10). That is due to the random choice of shape parameters C_n. However, since all of our conclusions are based on the final, optimal population, a possible lack of accuracy in the calculation of hydrodynamic forces in the initial generations is of little or no consequence. Repeated runs provide a large enough selection of slender bodies in the initial populations for the optimisation results to be valid. Similar arguments are valid for motion envelopes $r(x)$, figure S11

The relative body wave length $\lambda_b' \equiv \lambda_b/L$ is undoubtedly an important parameter influencing the swimming performance. However, Lighthill's theory is not valid for extreme values of λ_b', either large or small. For very small values of λ_b', the small motion assumption is not valid due to the steep waves of body deflection. For very large values of λ_b', the body motion approaches that of a rigid body for which the thrust should be zero if only added mass effects are considered. However, the thrust is non-zero in that case according to Lighthill's theory. When using λ_b' as an additional optimisation variable, the swimmers with
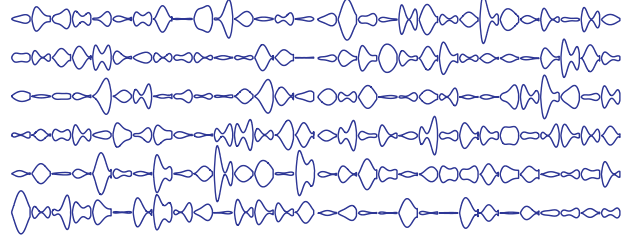

Figure S10: Some shapes from a random initial population. Lengths are made the same for easier comparison.
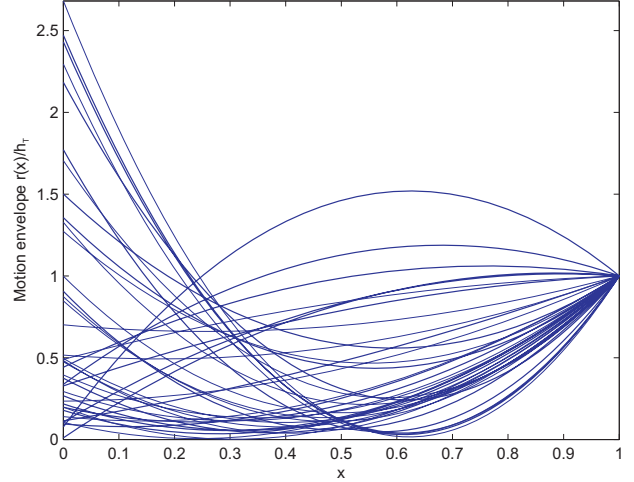

Figure S11: Some motion envelopes $r(x)$ of an initial random population. The motion envelopes have been normalised by the tail amplitude h_T for easier comparison.

small values of λ_b' are filtered out by the optimisation (for one, due to higher internal viscous losses). However, our tests have shown that larger values of λ_b' tend to propagate through the optimisation iterations and the optimal values reach the upper bound imposed on it. To prevent the optimisation from being stuck in regions where the theory is not valid, we do not use λ_b' as an optimisation variable and set $\lambda_b' = 1$.

5   The definition of cost of transport

Cost of transport COT is a measure quantifying the energy required to transport a kilogram of organism's mass over a unit distance [10, 16] and as such can be considered as an energetic measure of primary importance to an organism in motion. It is essentially "gallons-per-mile" measure ,

$$COT \propto \frac{E}{ml} \,, \tag{S.14}$$

where E is the *total* energy ("gallon") required for a body of mass m to travel the distance l ("miles"). A more common version of expression (S.14) can be obtained by dividing both the numerator and the denominator by the time τ required to traverse the distance l, giving

$$COT \propto \frac{E/\tau}{m\,l/\tau} = \frac{P_{tot}}{m\,U}\ , \qquad (S.15)$$

where P_{tot} is the average metabolic power required for swimming at steady speed U. To make the COT a non-dimensional measure, right-hand side of (S.15) is divided by g which gives the standard form of COT given by equation (8) in the main paper.

The division by g has no significance to any of the results since g is constant and the same for all organisms. Any constant quantity with the dimension of acceleration would serve the purpose equally well. Even if COT is left in the form of (S.15), the results presented in the main paper would be the same (apart from quantitative difference in COT). The division by g is used to conform with common practice and it is carried over from terrestrial locomotion, where is commonly used to compare the cost of transport of different vehicles [18]. However, the presence of g does not imply that gravity plays a role in swimming.

The ambiguity in making COT non-dimensional comes from the fact that COT was not obtained through the standard apparatus of dimensional analysis of quantities relevant to the swimming problem. Instead, it is introduced as a measure that is initially dimensional (consumed energy per unit mass and distance). Introducing problem relevant quantities to non-dimensionalise it (say by U^2/L) would change the initial intent of the measure. Non-dimensionalising by g preserves the meaning of the measure and gives some physical intuition about its values (energetic cost relative to the cost of lifting the same object with same speed against gravity).

6   Additional results

6.1   Comparison to a CFD study

Some of our results (figure 3 in particular) are somewhat different from the findings of a numerical study of the hydrodynamics of mackerel and lamprey swimming. Borazjani & Sotiropoulos [19] find that, in inviscid case, a mackerel swimming in carangiform pattern ($\lambda_b/L = 0.94$ in their case, with very similar motion envelope to $(r(x))_{COT-opt}$) is faster than a mackerel swimming in anguilliform pattern ($\lambda_b/L = 0.64$), and faster than a lamprey swimming in either carangiform or anguilliform pattern. In contrast, we find that for $m = 0.1$kg (mass approximately corresponding to Re at which mackerel and lamprey swim in nature) an organism that exhibits motion closest to mackerel's (figure 3) is actually COT-optimal and, thus, the slowest of all optimal organisms. Furthermore, COT-optimal shape is somewhat closer to mackerel, while U-optimal is closer to lamprey, figure 4.

The comparison of [19] with our results, however, cannot be made in a straight-forward manner. The comparison is limited to carangiform motions only since we limit our analysis to $\lambda_b/L = 1$, which is similar to $\lambda_b/L = 0.94$ used in [19]. The comparison is further made complicated by the difference in Re, since Re is the same for mackerel and lamprey in [19], while in our case Re is different for each organism. Furthermore, the absence of a muscle model in [19] questions the feasibility of the motion pattern they prescribe. While mackerel and lamprey swimming with their own natural pattern is feasible since it is copied from nature, it is not clear whether mackerel swimming with lamprey's (anguilliform) motion pattern, or lamprey swimming with mackerel's (carangiform) motion pattern, would be physiologically feasible at all as a muscle model is not used in [19]. The body shapes in the two studies are not identical, although COT-optimal and U-optimal organisms for $m = 0.1$kg are somewhat similar to mackerel and lamprey, respectively. The body lengths are in [19] are identical, while in our case COT-optimal and U-optimal organisms are of different length. These differences in body geometries between the two studies might also have an impact on how the results compare.

6.2 Kinematic and geometric characteristics of optimal organisms across the scales

The Fig. S12 shows further results complimenting those from the main text. The relative swimming speed U/L in body lengths per second, Fig. S12a, is a quantity that is often found in literature when discussing the swimming performance. The comparison of our predictions for U/L values closely match those found in nature. We have chosen to show U–m plot in the main paper because U is one of the objective functions and because some comparisons with results and conjectures from the literature involve U, not U/L [20, 21]. Furthermore, some constraints in our model (μ_{max}) refer to U, not U/L. Maximum relative contraction velocity $\max v_r$, Fig. S12c, is the maximum value that $v_r(x,t)$ attains over the tail-beat period and along the length. Since the tail-beat period T increases with the increase of m, the decrease of $\max v_r$ is correlated with the decrease of tail-beat frequency ω. This has also been empirically found for cyclical muscle contractions [22], offering further validation to our muscle model.
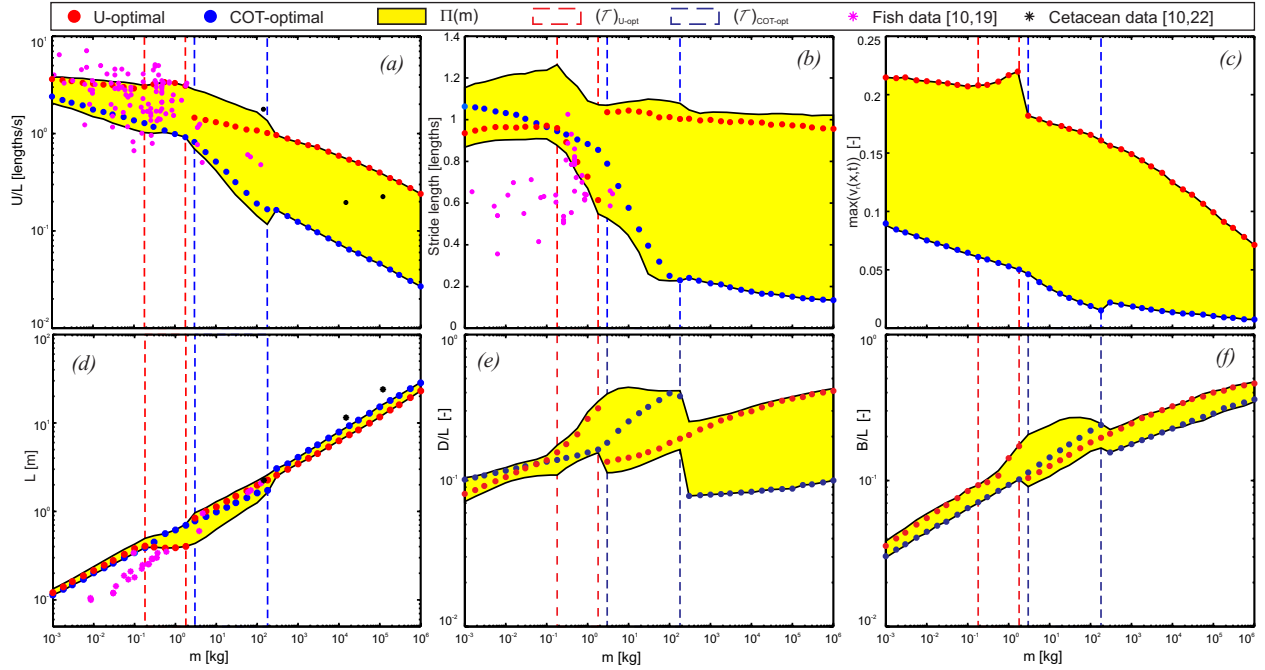
Figure S12: Kinematic and geometric characteristics of optimal populations $\Pi(m)$ compared to empirical data for fish [10, 20] (magenta stars) and cetaceans [10, 23] (black stars). Organisms with minimum COT are marked by blue circles and U-optimal organisms by red circles; the rest of $\Pi(m)$ are represented by yellow region(s). The transition region $(\mathcal{R}_T)_{U-opt}$ is marked by red dashed line and $(\mathcal{R}_T)_{COT-opt}$ by blue dashed line. Where mass measurements are missing, they are obtained from an $m - L$ allometric expression ($m = 12.62L^{3.11}$). (a) Relative speed U/L, in body lengths per second. (b) Relative stride length λ_S/L, in body lengths. (c) Maximum relative contraction velocity $\max v_r$. (d) Body length L. (e) Relative tail height D/L. (f) Relative body width B/L.

References

[1] Lighthill, M. J., 1960 Note on the swimming of slender fish. *J. Fluid Mech.* **9**, 305–317

[2] Boyd, J. P., 2001 *Chebyshev and Fourier spectral methods*. Dover, New York

[3] Deb, K., 2001 *Multi-objective optimization using evolutionary algorithms*. Wiley, New York

[4] Igel, C., Hansen, N. & Roth, S., 2007 Covariance matrix adaptation for multi-objective optimization. *Evol. Comput.* **15**, 1–28

[5] Videler, J. J. & Nolet, B. A., 1990 Costs of swimming measured at optimum speed: scale effects, differences between swimming styles, taxonomic groups and submerged and surface swimming. *Comp. Biochem. Physiol. A.* **97**, 91–99

[6] Hansen, N. & Ostermeier, A., 2001 Completely derandomized self-adaptation in evolution strategies. *Evol. Comput.* **9**, 159–195

[7] Hansen, N., Müller, S. D. & Koumoutsakos, P., 2003 Reducing the time complexity of the derandomized evolution strategy with covariance matrix adaptation (CMA-ES). *Evol. Comput.* **11**, 1–18

[8] Deb, K., Pratap, A., Agarwal, S. & Meyarivan, T., 2002 A fast and elitist multiobjective genetic algorithm: NSGA-II. *IEEE Trans. Evol. Comput.* **6**, 182–197

[9] Webb, P. W., 1975 *Hydrodynamics and energetics of fish propulsion*. Dept. of the Environment Fisheries and Marine Service

[10] Videler, J. J., 1993 *Fish Swimming*. Chapman & Hall, London

[11] Syme, D. A., Gollock, M., Freeman, M. J. & Gamperl, K. A., 2008 Power isn't everything: Muscle function and energetic costs during steady swimming in Atlantic Cod (Gadus morhua). *Physiol. Biochem. Zool.* **81**, 320–335

[12] Syme, D. A., 2006 Functional properties of skeletal muscles. In *Fish Biomechanics: Fish Physiology*, volume 23 (eds. R. E. Shadwick & G. V. Lauder), pages 179–240. Academic Press, New York

[13] Alexander, M. R., 1997 Optimum muscle design for oscillatory movements. *J. Theor. Biol.* **184**, 253–259

[14] Curtin, N. A. & Woledge, R. C., 1993 Efficiency of energy conversion during sinusoidal movement of red muscle fibres from the dogfish Scyliorhinus Canicula. *J. Exp. Biol.* **185**, 195–206

[15] Webb, P. W., 1971 The swimming energetics of trout: II. Oxygen consumption and swimming efficiency. *J. Exp. Biol.* **55**, 521–540

[16] Wu, T. Y., 1977 Introduction to the scaling of aquatic animal locomotion. In *Scale Effects in Animal Locomotion* (ed. T. J. Pedley), pages 203–232. New York: Academic Press

[17] Schultz, W. & Webb, P. W., 2002 Power requirements of swimming: Do new methods resolve old questions? *Integr. Comp. Biol.* **42**, 1018–1025

[18] Gabrielli, G. & von Karman, T., 1950 What price speed? *Mech. Eng.* **72**, 775–781

[19] Borazjani, I. & Sotiropoulos, F., 2010 On the role of form and kinematics on the hydrodynamics of self-propelled body/caudal fin swimming. *J. Exp. Biol.* **213**, 89–107. (doi:10.1242/jeb.030932)

[20] Block, B. A., Booth, D. & Carey, F. G., 1992 Direct measurement of swimming speeds and depth of blue marlin. *J. Exp. Biol.* **166**, 267–284

[21] Webb, P. W., 1994 Exercise performance of fish. In *Advances in veterinary science and comparative medicine*, volume 38B, pages 1–49. Academic Press

[22] Askew, G. N. & Marsh, R. L., 1998 Optimal shortening velocity (V/Vmax) of skeletal muscle during cyclical contractions: length-force effects and velocity-dependent activation and deactivation. *J. Exp. Biol.* **201**, 1527–1540

[23] American Cetacean Society Fact Sheet, 2010. http://www.acsonline.org/factpack/bluewhl.htm